Schlichting and Kersten *EPJ Techniques and Instrumentation* (2023) 10:19
https://doi.org/10.1140/epjti/s40485-023-00106-4
EPJ.org
EPJ Techniques and Instrumentation

RESEARCH ARTICLE

Open Access

A retarding field thermal probe for combined plasma diagnostics

Felix Schlichting[1*] and Holger Kersten[1]

*Correspondence:
schlichting@physik.uni-kiel.de
[1]Institute for Experimental and Applied Physics, Kiel University, Leibnizstraße 19, 24098, Kiel, Germany

Abstract

The wide variety and ever-growing applications of plasma processes in research and industry require an equally growing diversity and accessibility of suitable plasma diagnostics. The plasma parameters and the tailoring thereof strongly influence the outcome of thin film deposition, plasma etching, or surface treatments, to name only a few. To further enhance the determination of different fluxes of species, their energies, and behaviour influencing a surface process, a custom-built combination of two commonly used diagnostics was developed. With a retarding field energy analyzer, one can obtain the ion energy distribution in a plasma by measuring the current at the collector depending on the applied voltage at the scan grid. A passive thermal probe determines the energy flux density coming from a process plasma by measuring the temperature change of a dummy substrate. In this study, we present a retarding field energy analyzer where a passive thermal probe substitutes the collector. By doing so, we can determine the energy distribution of the charged ions, their energy flux density at a certain potential, and the power deposited onto a substrate. Another advantage is that the thermal probe can even measure the power deposited by incoming (fast) neutrals and of the background gas when the grids keep away the ions. Hence, combining these two powerful diagnostics yields information neither can deliver on their own. The probe has been tested in three different plasma environments: ion beam source, magnetron sputtering and radio frequency discharge plasma.

Keywords: Plasma diagnostic; Diagnostic combination; Ion energy distribution; Energy flux density; Energy balance

1 Introduction

In plasma diagnostics, one can rely on a wide variety of options depending on the investigated discharge environment. The external parameters such as gas pressure, gas flow, discharge geometry and applied power determine the internal parameters of that environment. These include the potential and kinetic energies of the involved particles (electrons, ions, neutrals and possibly precursor radicals) and the energy these particles transfer to a surface as well as the potentials within the plasma and the force the plasma exerts on a surface [1]. Plasma diagnostics such as optical spectrometry [2], mass spectrometry [3], electrical probe diagnostics [4] or sensitive mechanical probes [5] are commonly used to determine critical plasma parameters.

The focus of this work is on electrical and thermal probes. Electrical probes are commonly used to measure plasma parameters such as plasma potential, electron density and electron temperature, ion energy distribution and magnetic field strength. An important example of these diagnostics is the Langmuir Probe, which, despite its simple design, or maybe just because of it, can be used in many different plasma environments [6–8]. Another example is the hairpin probe, which analyzes the amplitude and phase of the rf voltage and current in a resonant circuit [9]. Magnetic probes measure the magnetic field strength and direction in the plasma [10] and the retarding field energy analyzer is used to determine the ion energy distribution [11]. Thermal probe diagnostics help study plasma-surface interactions, plasma chemistry, and plasma processing. Examples are bolometers, which are primarily used in confined fusion devices [12]. Additionally, various types of calorimetric probes exist using thermocouples and temperature measurements to determine energy fluxes onto surfaces in a plasma, based on the principle introduced by Thornton [13]. They can be used to understand better the plasma behaviour for applications such as plasma etching, thin film deposition, and modification.

Recently, novel and not state-of-the-art methods have been performed. For example, there are thermionic probes, mainly used in magnetically confined fusion devices [14], and optical probes using lasers as trapping systems [15] or Thompson scattering [16], laser-induced fluorescence [17] or microwave interferometry [18].

Most of these diagnostics are invasive, meaning that they change or, at least, minimally disrupt the plasma environment by introducing them. On their own, they often have limitations concerning the probe placement and obtained results. To get a more comprehensive understanding, multiple diagnostics are often deployed separately. The ever-growing complexity of the processes in which plasmas are used calls for more multilateral components, which can get results out of minimal invasion, which led to the idea of combining existing diagnostics.

2 Plasma diagnostics

The two diagnostics will be discussed separately to understand the abilities better (but also shortcomings) of the suggested combined probe techniques. Since both diagnostics are well-known and established, we will not go into too much detail.

2.1 Retarding field energy analyser

Different routes exist to design a retarding field energy analyzer (RFEA) depending on the requirements for the plasma process investigated. In principle, it consists of vertically aligned grids acting as filters or lenses for an incoming charged particle flux. As shown in Fig. 1a, the most commonly used is a three- to four-grid system.

Grids G1, G2, and G3 are designated as the screen grid, scan grid, and secondary electron repeller grid (SE repeller), respectively. Grid G0 is optional. Depending on the size of the orifice Or, one may use an extra grounded Grid G0 to change the electrical field in front of the RFEA and prevent, i.e. the bulk plasma in an rf capacitively coupled plasma (rf-ccp) from spreading into the probe. The voltages applied to the different grids are schematically shown in Fig. 1b.

The negative bias at the screen grid prevents electrons from entering the RFEA. Positive ions can pass the scan grid in proportion to the applied voltage ramp, and the resulting

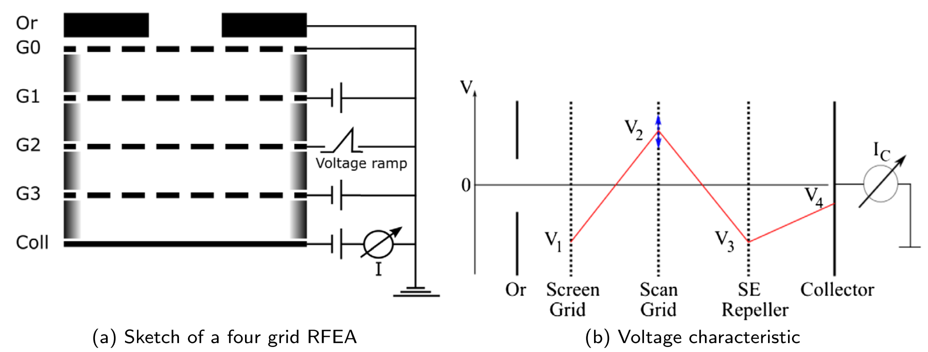

Figure 1 (a) Or: orifice; G0: grounded grid; G1: screen grid; G2: scan grid; G3: secondary electron (SE) repeller; coll: collector plate; (b) The static voltages *V*1, *V*3 and *V*4 applied to the respective grids and the voltage ramp barrier *V*2, as usually used by an RFEA

Figure 2 Typical RFEA measurement and differentiated collector current, resulting in the ion energy distribution (IED)

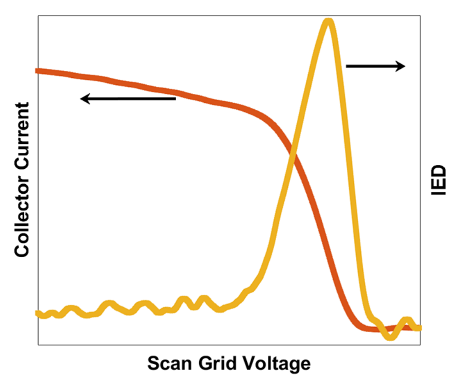

current I_C is measured at the collector. Upon impact, the ions can release secondary electrons (SE) from the collector, distorting the measured current. Therefore, $V3$ must have a larger bias than the collector to repel the SEs.

Measuring the voltage ramp and the resulting collector current yields the typical I-V characteristic from which the ion energy distribution (IED) can be calculated by differentiating the curve, as exemplified in Fig. 2. The ion velocity distribution, and therefore their kinetic energy, is related to the collector current I_C and the scan grid voltage U_S [19, 20] like the following

$$f(v) \propto \frac{dI_C}{dU_S}. \tag{1}$$

By simply differentiating the I-V characteristic, the obtained IED indicates how many ions per unit of time and area are hitting the surface of the collector. A precise determination of the ion energy/velocity distribution is not given at this point. This would require an exact knowledge of the transparency of the grids and the influence the distance of the collector has on the measured current. Exact calibration of the combined probe will be done in the future. Here, the IED will be displayed in arbitrary units.

With the possibility of using a different number of grids and spacing them individually, the RFEA is a widely used tool to investigate ion energy distribution in a plasma [11, 21, 22].

But as soon as the electron energies and velocities, neutral fluxes or overall energy flux densities of species are of interest, additional diagnostics are necessary.

2.2 Passive thermal probe

The passive thermal probe (PTP) and the actual design used in these experiments have been presented elsewhere [23, 24]. The probe consists of a substrate dummy with a diameter of 11 mm. A 100 μm thick copper plate is usually used as substrate. One might use different materials with a higher or lower heat capacity, depending on the incoming energy flux density. The temperature measurements used to determine the incoming integral energy flux are obtained via a Type K thermocouple, which is spot-welded to the back of the substrate dummy. A shielded copper wire is additionally welded to the plate to bias the probe and perform current measurements.

By measuring the temperature change of the probe set off by exposing it to a plasma source, a time and energy-integrated value of the energy flux density can be obtained. The evaluation procedure is described in detail in [25]. The typical temperature evolution of the probe during plasma exposure is shown in Fig. 3. It can be divided into two phases: the heating phase and the cooling phase. During the heating phase, the plasma source is on and the overall change in enthalpy $\dot{H}_h$ of the probe is dominated by the incoming power P_{in}. Charged and neutral particles impinging on the substrate, surface processes like film formation, secondary electron emission, or relaxation of metastable atoms or molecules, as well as heat radiation from a target or chamber walls are the origin for the incoming power (energy influx).

When the plasma source is switched off, the substrate cools down, and its change in enthalpy $\dot{H}_c$ is now solely governed by the outgoing power (cooling) $P_{out,c}$. These two phases can be written as:

$$\dot{H}_h = C_s\,\dot{T}_h = P_{in} - P_{out,h}, \tag{2}$$

$$\dot{H}_c = C_s\,\dot{T}_c = -P_{out,c}, \tag{3}$$

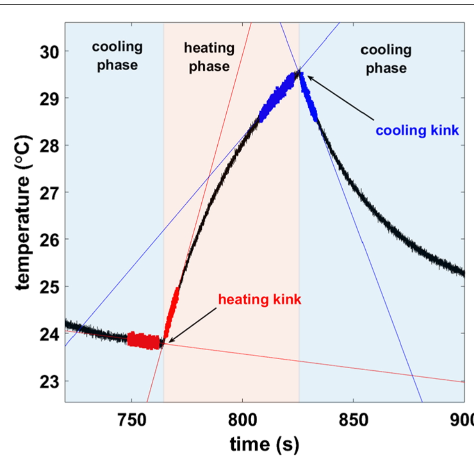

Figure 3 Exemplary depiction of the two phases and the change in temperature of the PTP over time in a magnetron sputter deposition chamber

C_s is the heat capacity of the probe, which can be determined by electron beam calibration [24]. $P_{out,h}$ is the outgoing power during heating. $\dot{T}_h$ and $\dot{T}_c$ are the time derivatives of the temperature during the heating and cooling phases, respectively.

We only examine short periods around the two kinks shown in Fig. 3. Here, we can assume that the outgoing power during the respective phases is always the same. Therefore, we can combine equations (2) and (3) to calculate the incoming energy flux density $J_{in,exp}$:

$$J_{in} = \frac{P_{in,exp}}{A_s} = \frac{C_s}{A_s}\,(\dot{T}_h - \dot{T}_c), \tag{4}$$

where A_s is the probe surface area. The linear fits are made around the kinks to determine $(\dot{T}_h - \dot{T}_c)$ for each of the kinks. From this difference, a mean is obtained as the energy flux density.

2.3 Combination of both diagnostics: RFEA and PTP

The passive thermal probe has been used in a wide range of environments from low-pressure process plasmas such as rf-ccp sources to high power impulse magnetron sputtering (HiPIMS) systems and ion beam sources or atmospheric pressure plasmas [26–29]. It has proven to be a versatile diagnostic, and with the ability to bias the probe, it can even be used as a planar Langmuir probe, as shown in [27]. The possibility to apply a bias voltage and to measure the current to the probe led to the idea that this probe should also qualify to be used as a collector in an RFEA system, where it simultaneously would allow the measurement of the incoming energy flux density from a plasma source depending on the scan grid voltage of the RFEA.

For this purpose, the former PTP design [25] was modified to place the grid system in front of the substrate plate, as shown in Fig. 4a. The grid holder is made from a thermoplastic polymer (PEEK) and fixed on the PTP base. PEEK is thermostable up to around 340°C and electrically and thermally insulating. It is also relatively cheap and can be easily machined with a CNC cutter, thus making it a very suitable material. An expanded and detailed view of the grid holder with the individual grids is displayed in Fig. 4b. The secondary electron repeller grid is positioned directly above the grid holder. Scan grid and screen grid are rotated 90° to each other. This way, the protruding latches of the grids can be led to the sides of the holder and connected to the electrical measurement system. Optionally, a fourth grounded grid can be placed in front of the screen grid, as explained above and shown in Fig. 1b.

The grids have a thickness of 0.2 mm, the same as the grid cutout in the placer. The placers have a thickness of 0.5 mm, which leads to a grid-to-grid distance of 0.3 mm. In hexagonal order, the grid holes have a diameter of 0.4 mm and a 0.5 mm centre-to-centre distance, thus creating a 58% optical transparency for each grid. As a whole, the combined diagnostic will now be referenced in the text as a retarding field thermal probe (RFTP).

To adapt the measurement principle of the two separate diagnostics and to be able to combine them, one has to consider that a single RFEA scan may take only a few seconds, whereas, in contrast, the PTP measurement may take minutes. The time for the required heating and cooling phases depends on the incoming energy flux and the plasma conditions. With an ion current onto the PTP/collector of only a few mA, which is reduced further with rising scan grid voltage, it can take around 30 seconds to heat the PTP a few

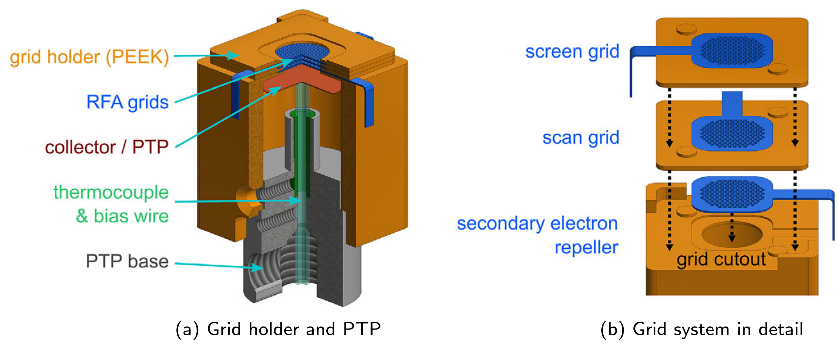

Figure 4 (a) PTP base with grid holder, RFA grids, collector/PTP, and wiring; (b) Expanded view of the grid holder. The grids are fitted into the grid cutouts of the individual placers

Figure 5 RFTP with water-cooled housing. The housing and orifice cap is made of stainless steel

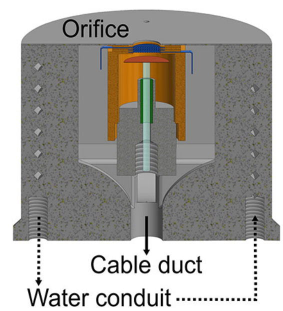

degrees. The respective cooling phase also depends on the environment. The cooling becomes significant considering the housing of the RFTP.

To shield the latches of the grids and the attached wiring from the plasma, the setup in Fig. 4a is placed in a stainless steel housing. When exposed to plasma for longer periods, the housing can heat up so much that the heat radiation affects the PTP and thereupon acts as an unquantifiable energy source distorting the measured temperatures. This would even lead to the probe's heating during the cooling phases. Therefore, the housing can be water-cooled, as depicted in Fig. 5. The housing is 3D-printed stainless steel with a circular water conduit. Once the housing is cooled down, the low thermal conductivity of stainless steel shields the PTP from outside heat sources. Through the cable duct, all wiring can be routed out of the vacuum chamber via a rotary feed-through. The orifice cap is screwed on top of the housing and serves simultaneously as the ground connection to grid G0 (Fig. 1a).

As mentioned in the previous chapter, different sizes and materials can be used for the PTP substrate. The standard 11 mm copper platelet has a heat capacity of around 0.03 J/K. When the incoming ion current is relatively small, leading only to a slight change in temperature of the probe (collector), experiments are performed with a Tantalum substrate of 5 mm diameter, resulting in a lower heat capacity of $C_S = 0.00758 \pm 0.00017$ J/K. This enables the probe to respond more sensitively to small temperature changes.

3 Examples for experimental tests of the RFTP

The idea of the cooled housing is to stabilize the temperature inside the RFTP and of the PTP substrate so that the outgoing power from the PTP during the measurement is

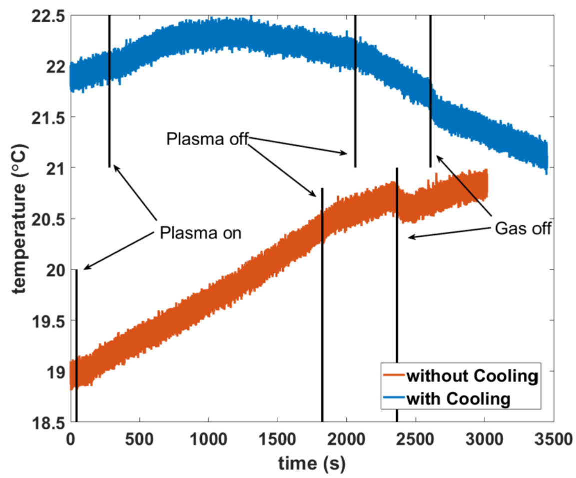

Figure 6 Temperature courses of the PTP substrate with and without water cooling of the housing. Vertical lines indicate event times

Figure 7 The RFTP (purple) is embedded into the grounded electrode. The bias cable of the PTP is connected to the collector output of the RFEA electronics. The screen grid, scan grid and SE repeller are wired directly

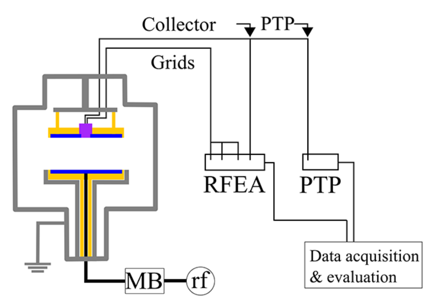

constant and that there are no external heating sources other than the incoming ions or neutrals passing through the RFEA.

To demonstrate this effect, Fig. 6 shows temperature evolution with and without water cooling, respectively. The RFTP was embedded in the grounded electrode of an rf-ccp parallel plate discharge in an argon plasma, shown in Fig. 7. The powered electrode was driven with 50 W, the plasma was ignited for 30 minutes, and after another 10 min, the gas was turned off. During the measurements, there was no voltage applied to the RFEA grids. Without cooling, there is an almost linear increase in temperature. The temperature still rises after the plasma and even after the gas is turned off. In contrast, a cooled housing results only in a minimal temperature change while the plasma is ignited and cools the probe afterwards. The probe will be cooled to the equivalent temperature depending on the water temperature. Since this cooling factor stays constant throughout all measurements, it can be ignored for evaluating the PTP temperature courses.

Returning to the duration of the two diagnostics mentioned in the previous chapter, it is now possible to have sufficient time to cool the PTP and determine the incoming energy flux of ions passing through the RFEA for a given grid voltage configuration. Hence, to obtain corresponding RFEA and PTP data, a standard RFEA scan is performed, and then PTP measurements are performed for fixed scan grid voltages in well-defined steps. At the same time, the other grid voltages remain constant. Then, the ion current to the collector and the energy flux density can be compared for the corresponding scanning range. In the following, such measurements are shown for several discharge conditions.

The electronic devices for temperature, voltage, and current measurements are custom-built. Figure 7 shows the probe embedded into the grounded electrode of the rf plasma chamber with the cables and measurement setup. The PTP has its own electronic and vacuum feed-through. The additional BNC bias cable is separated from the temperature measurements and can be connected to the collector output of the RFEA electronics. The RFEA electronic has four BNC outputs for the three grids and the collector, with two outputs for fixed voltages (screen grid and SE repeller) and two outputs with additional possibilities of current measurements and sweeping bias voltages.

3.1 Ion beam

Measurements were performed in an ion beam for a distinct and controlled environment regarding ion energy and plasma density. Here, ions and electrons are produced in an electron cyclotron resonance (ECR) discharge as described in [30]. With the use of an anode ring around the discharge, the ions can be accelerated up to U_{anode} = 1200 V. Two different setups were used: the smaller vertically aligned source (VIB) [31] and a larger horizontal ion beam (HIB) [32].

3.1.1 Vertical ion beam

Figure 8 shows typical measurements in the vertical setup. Here, the distance of the RFTP to the ion source cannot be changed due to geometrical limitations and is about 0.2 m.

The RFTP is placed in the chamber's centre facing the ion beam, and the orifice is changed to 4 mm diameter. The grounded grid is left out. Figure 8a shows the RFEA measurements in the same way as discussed in the previous chapter. The maximum measured ion current is roughly 30 μA, much higher than in an rf plasma. The total energy of the ions is $E_{ion} = e(U_{anode} + U_{pp1} - U_{pp2})$ [32]. The sheath potential drop in the ion source is $U_{pp1} = +(60 \pm 10)$ V. The plasma potential of the secondary plasma $U_{pp2} = +(15 \pm 5)$ V in the chamber is highly dependent on the working gas pressure and the anode voltage of the source [31]. This can be seen in the RFEA measurements in Fig. 8a, where the peak of the IED is at approximately 360 V whereas the anode voltage is U_{anode} = 300 V. Of course, not all ions and their potential energy are wholly affected, leading to the plateau in the IED and the rather large width of the distribution.

The measured energy flux density (EFD), seen in Fig. 8b, also drops at the same voltage as the ion current. It amounts to roughly $J_{in,max} = 1.45 \pm 0.09$ mW/cm^2 (average of measurement points of the PTP for scan grid voltage < 300 V). Looking at Fig. 8b the residual EFD above 375 V scan grid voltage is at around $J_{in,min} = 0.38 \pm 0.06$ mW/cm^2 (average of measurement points for scan grid > 360 V). This residual energy flux density can be attributed to fast neutrals originating in charge exchange collisions.

The charge exchange collisions of the ions in the beam with the background gas atoms result in fast, energetic neutral atoms. For ions with energies $E_i > 100$ eV the approximated net cross section for these collisions is $\sigma_{cx}(E_i) = 5.75 \cdot 10^{-19}(E_i/eV)^{-0.1}$ m^2 [31] when using the energy dependent cross sections given by Phelps [33]. For ions with an energy of E_{ion} = 360 eV and gas pressure of $2.6 \cdot 10^{-2}$ Pa, the mean free path for charge exchange collisions was determined to $\lambda_{cx,vib} = 0.49$ m.

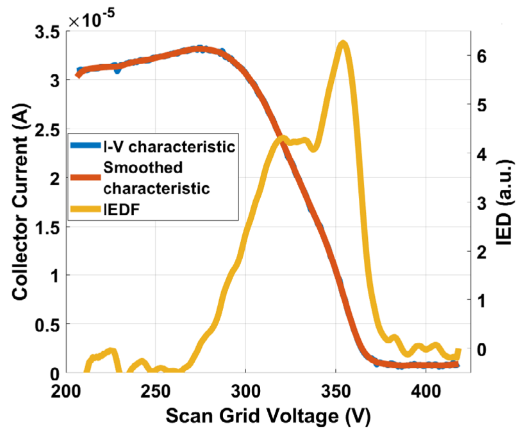

(a) RFEA measurement in vertical ion beam experiment

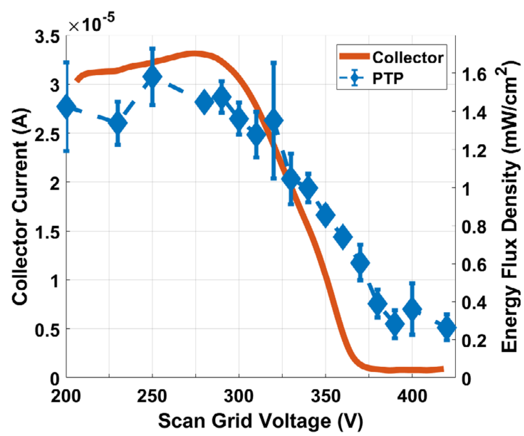

(b) Corresponding energy flux density with measured collector current

Figure 8 RFEA (a) and RFTP (b) measurements in a vertical ECR ion beam. The working gas is argon at $2.6 \cdot 10^{-2}$ Pa. The anode voltage of the source is $U_{anode} = 300$ V

Assuming that only ions and fast neutrals contribute to the total energy flux density J_{in}, the contribution of ions will be [31]

$$\frac{J_{in,ions}(z)}{J_{in,max}(z)} = \exp\left(-\frac{z}{\lambda_{cx,vib}}\right) = 0.66 \tag{5}$$

for $z = 0.2$ m. The proportion calculated with the measured energy flux density from Fig. 8b is

$$\frac{J_{in,max} - J_{in,min}}{J_{in,max}} = 0.74 \pm 0.04 \tag{6}$$

which is in good accordance with the theoretical approximation. Hence, the energy flux density due to the ions is $J_{in,ions} = 1.07 \pm 0.07$ mW/cm^2.

The proximity to the ion source did not allow measurements above the aforementioned anode voltage. The ion beam plume pushes too much into the RFTP for larger energies. The growing space charge between the grids of the RFEA can result in breakdowns between the screen and scan grid.

3.1.2 Horizontal ion beam

A second ion beam setup was investigated to avoid this problem. Here, the ion source is oriented horizontally inside a larger vacuum vessel with a length of 1.6 m and a diameter of 0.65 m [32]. The RFTP can be placed at the opposite end in the centre, facing the ion beam. A rod alters the distance, which also serves as the cable feed-through. Applying up to 750 V to the anode was possible in this setup. The distance of the RFTP to the ion source was $z = 0.9$ m. The measurements are shown in Fig. 9.

The larger distance to the source allowed for higher ion energies to be investigated. The ion beam, however, diverges in its diameter as it extends further into the chamber. This can be observed in Fig. 9a, where the collector current drops from around 700 V until the scan grid voltage reaches 900 V. There are two peaks in the IED at 750 V and 880 V and the plateau is much more pronounced compared to the VIB measurements. There is no reasonable explanation for this higher energy of the ions in the beam. A thermionic cathode has been placed before the ion beam source to prevent breakdowns inside the chamber. However, this could not fully be averted, which leads to a distortion (small peaks) in the measured collector current, which can be seen in the upper left corner of Fig. 9a in the collector current. Measurements taken for lower anode voltages reveal that the apparent high energy peak shifts to higher scan grid voltages and gets more pronounced if the anode voltage is higher. Figure 10 shows the measured ion energy distributions for anode voltages of 300 V, 500 V, 600 V and 800 V. Additionally, the measured I-V characteristic for $U_{anode} = 800$ V is displayed. Again, small peaks from breakdowns inside the chamber can be observed, especially around scan grid voltages of 900 V, leading to this pronounced peak in the corresponding IED. This also indicates some limitations of the probe concerning the hole diameter of the grids and the grid distance in the RFEA system.

In the following, the ion energy will be taken from the first peak in Fig. 9a. In the horizontal ion beam experiment, the plasma potential inside the source is $U_{pp1} = +(60 \pm 10)$ V, since this setup uses the same ECR plasma source as in the VIB. The plasma potential in the chamber, however, is found to be $U_{pp2} = +(40 \pm 10)$ V [32], measured for an anode potential of $U_{anode} = 1200$ V. Therefore, the total ion energy in this setup would be expected to be around the anode potential. The energy flux density taken from the PTP measurements in Fig. 9b follows the collector current. Here, in contrast to the vertical ion beam experiment, the residual EFD is still significantly higher. For ions with an energy of 750 eV and gas pressure of $1.76 \cdot 10^{-2}$ Pa, the mean free path for charge exchange collisions comes to $\lambda_{cx,hib} = 0.79$ m. This results in a partial contribution of the ions to the energy flux density of

$$\frac{J_{in,ions}(z)}{J_{in,max}(z)} = \exp\left(-\frac{z}{\lambda_{cx,hib}}\right) = 0.32 \tag{7}$$

for $z = 0.9$ m. The maximum EFD is 8.79 ± 0.45 mW/cm^2 (averaged over the first seven measurement points for scan grid voltage < 700 V) above the remaining 6.27 ± 0.12 mW/cm^2 (averaged over the four last measurement points for scan grid > 900 V). This results in a measured ion contribution of

$$\frac{J_{in,max} - J_{in,min}}{J_{in,max}} = 0.28 \pm 0.04. \tag{8}$$

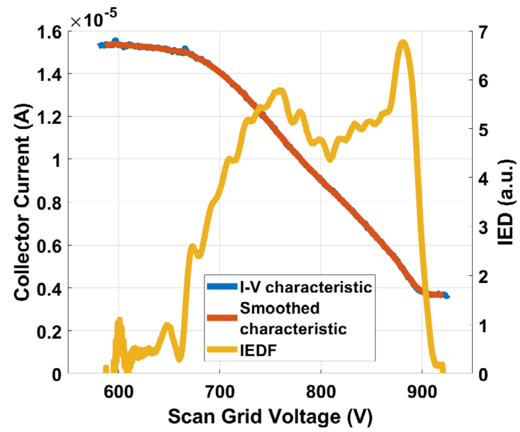

(a) RFEA measurement in horizontal ion beam experiment

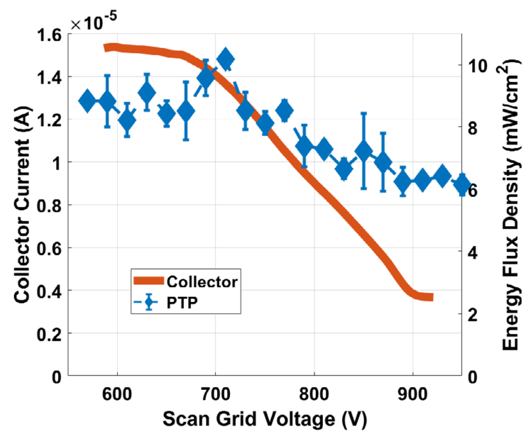

(b) Corresponding energy flux density with measured collector current

Figure 9 RFEA (a) and RFTP (b) measurements in a horizontally orientated ECR ion beam source. The working gas is Argon at $1.76 \cdot 10^{-2}$ Pa. The anode grid voltage of the source is 750 V

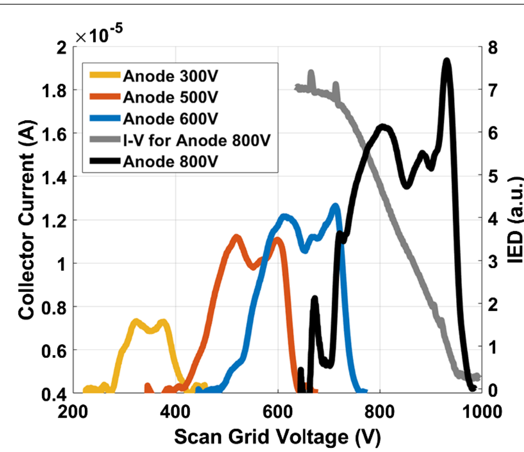

Figure 10 Measurements for different anode voltages showing the effect of breakdowns inside the chamber on the measured current and, subsequently, the IED

The contribution of ions to the maximum energy flux density coming to the collector is $J_{in,ions} = 2.5 \pm 0.3$ mW/cm^2. Axial Faraday cup measurements in this setup provide an ion beam current density of $j_{beam,FC} = 1.2$ μA/mm^2 for $z = 0.86$ m and $U_{anode} = 800$ V [34]. The orifice of the RFTP used in the HIB experiment has a diameter of $d_{or} = 6$ mm. Taking the maximum ion current measured at the collector of the RFTP from Fig. 9 as $I_{coll,max} = 15$ μA, the ion current density measured at the collector is $j_{coll} = I_{coll,max} / A_{or} = 0.53$ μA/mm^2. Since the experimental conditions are comparable, the electrical transparency of the RFTP approximately is $j_{coll} / j_{beam,FC} = 44\%$. The transparency will be higher if we consider the smaller distance and higher anode voltage with which the Faraday cup measurements were obtained.

3.2 Magnetron discharge

Next, measurements are performed in a high-power impulse magnetron sputter (HiPIMS) system [35]. The target cathode is operated with an 800 W DC power supply. The measurement electronics is not equipped to deliver a time resolution for a single pulse in such a system. A carbon target was used in an argon atmosphere at 0.36 Pa. The distance of the RFTP to the rectangular 10 × 30 cm carbon target is 10 cm. A 6 mm orifice of the RFTP was used.

For all magnetron discharge configurations that are used in a wide variety of scientific and industrial applications for processing substrate surfaces (e.g. thin film deposition in microelectronics or hard coatings), the energy balance at the substrate of arriving species (charged or neutral) is of utmost importance [36–39].

The film forming neutral atoms, which are ejected from the target surface, mainly influence the properties of the desired films. The energy needed for surface diffusion influencing the film's structure [40] mainly comes from bombarding ions of the inert working gas [41]. For these considerations, the RFTP enables the user to determine the energy balance between ions and neutrals at a specific location.

Examples of related measurements are shown in Fig. 11. The incoming energy flux density is at a maximum of $J_{in,max} = 1.06 \pm 0.09$ mW/cm^2 and only $J_{in,min} = 0.18 \pm 0.03$ mW/cm^2 still above 25 V scan grid voltage when the probe repels all charged species. This results in an ion-to-neutral ratio of

$$\frac{J_{in,max} - J_{in,min}}{J_{in,max}} = 0.83 \pm 0.03. \tag{9}$$

When looking only at charge exchange collisions, as in the previous chapter, the mean free path for charge exchange collisions is $\lambda_{cx,ms} = 0.27$ m. With this estimation, the partial contribution of ions to the total energy flux density would be

$$\frac{J_{in,ions}(z)}{J_{in,max}(z)} = \exp\left(-\frac{z}{\lambda_{cx,ms}}\right) = 0.69 \tag{10}$$

for $z = 0.1$ m.

The ratio discrepancy is expected since other collisions, especially elastic collisions, play an essential role in magnetron discharges. In addition to low-energy argon ions and neutral argon atoms impinging on the substrate (collector), other species, such as carbon ions or carbon clusters from the target, may also be present in the plasma and can arrive at the substrate. This, of course, depends on the magnetron discharge's operating conditions.

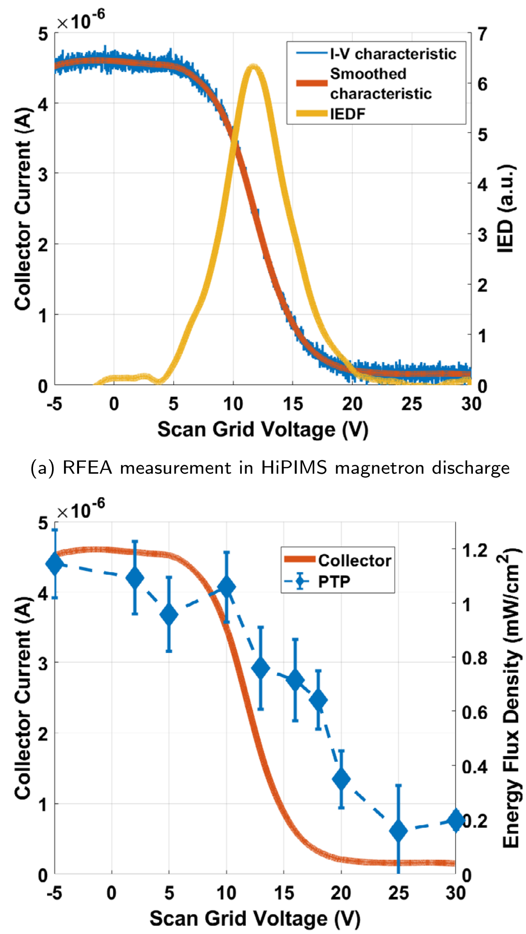

(a) RFEA measurement in HiPIMS magnetron discharge

(b) Corresponding energy flux density with measured collector current

Figure 11 RFEA (a) and RFTP (b) measurements in a HiPIMS system. The working gas is argon with 0.36 Pa with 55 sccm gas flow. The carbon target was operated at 800 W DC

To estimate the contribution of each of these species to the energy balance at the substrate (collector), one could resort to simulations using, for example, a binary collision approximation Monte-Carlo method. Up to now, these kinds of simulations are mainly used to discuss the thin film properties of ex-situ examined film deposited under corresponding conditions [39, 42, 43]. Hence, the RFTP can be a helpful link between simulations and ex-situ examined films, as it provides quantifiable and localized measurements of ion and neutral energy flux densities.

3.3 RF plasma

Last, measurements have been performed in an rf-ccp parallel plate discharge. The RFTP is embedded into the grounded electrode. The RFTP orifice has a 6 mm diameter, and the grounded first grid G0 shields the bulk plasma from the grid system. Grounded and powered electrodes are in a distance of 5 cm, and the powered electrode is driven with a 13.56 MHz voltage at 100 W power. The working gas is argon at a 2 Pa pressure.

Figure 12 shows typical measurements for a scan grid sweep from 0 V–50 V. Figure 12a shows the I-V characteristic, i.e. the collector current depending on scan grid voltage.

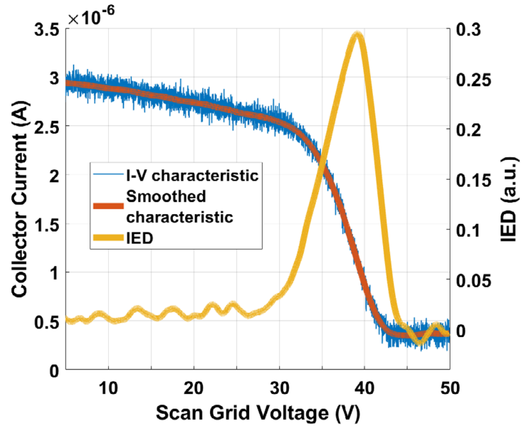

(a) RFEA measurement in rf-ccp parallel plate plasma environment. Operating pressure is 2 Pa Argon, and power is 100 W at driven electrode

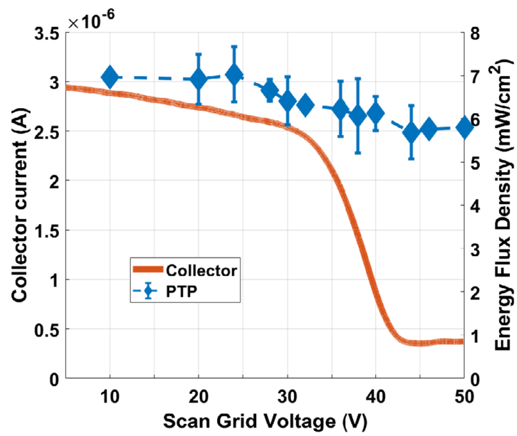

(b) Corresponding energy flux density with measured collector current

Figure 12 RFEA (a) and RFTP (b) measurements in rf-ccp parallel plate discharge

Also shown is the smoothed characteristic, resulting from a spline fit method, and the ion energy distribution (IED). Figure 12b shows the measured energy flux density (EFD) and the collector current. The energy flux arriving at the collector decreases with the rising scan grid voltage. Ions are steadily reflected at the scan grid, and the measured current drops. Simultaneously, the incoming energy due to energetic ions drops with the ion current. However, unlike the collector current, there is still a significant amount of energy flux $J_{in,min} = 5.75 \pm 0.06\ \mathrm{mW/cm^2}$ measured above 40 V, even though the charge carriers are blocked from the collector. The incoming EFD drops from $J_{in,max} = 6.97 \pm 0.06\ \mathrm{mW/cm^2}$ to $5.75\ \mathrm{mW/cm^2}$.

Since the RFTP housing is at a constant temperature, additional heat radiation from the holder can be ruled out. Of course, some heat radiation from the plasma might reach the PTP. Still, the remaining EFD comes from fast neutrals of the plasma bulk originating in charge exchange collisions and possibly a small percentage of recombined ions. Measurements with a cylindrical Langmuir probe inside the plasma bulk revealed a plasma potential of $\Phi_{Pl} = 30$ V and an electron density $n_e = 2.9 \cdot 10^{16}\ \mathrm{m^{-3}}$. The plasma potential is a good indicator for the RFEA measurements as the ions are accelerated, which is indicated by their energy distribution. Typically, rf plasmas have relatively low ionization rates, shown by the rather small electron density. This, however, confirms why the remaining EFD should come from neutrals passing through the RFEA grid system at such a high rate.

As was also discussed for the magnetron discharge, different types of energetic collisions are responsible for the remaining incoming energy flux $J_{in,min}$. Elastic collisions of ions with neutral gas molecules in the sheath can lead to energy loss and broadening of the ion energy distribution.

Within the plasma itself, charge exchange collisions can lead to the formation of fast neutrals. Overall, the EFD is much higher than in magnetron discharge, as well as the relationship between ion and neutral contribution, which is

$$\frac{J_{in,max} - J_{in,min}}{J_{in,max}} = 0.18. \tag{11}$$

The influence of collisions is much more pronounced, and (fast) neutrals dominate the energy balance at the grounded electrode.

4 Conclusions

The newly designed plasma diagnostic probe presented here opens up new possibilities in analyzing the energy spectrum of particles and flows in a broad range of different plasma environments. Ion energy distribution functions can be determined and correlated to their energy flux density. The measured energy flux density of (fast) neutrals originating from charge exchange collisions can also be determined. The PTP measurements require a steady environment where only the examined plasma contributes to changes in the temperature of the probe. This issue was solved using a water-cooled housing for the grid system and PTP.

In the case of ion beam experiments, where charge exchange collisions are essential, the measurements coincide with the theoretical model estimating the contribution of ions to the maximum measured EFD. Two different ion beam experiments were investigated. The distinction between ion and neutral contribution could very well be made. However, a precise determination of the ion energy was difficult, due to problems with the distance of the probe or breakdowns inside the chamber. Also, the resolution of the probe is still to be enhanced in the future. For plasma environments where elastic and other collisions play a more dominant role, the individual contributions of collisions to the overall energy balance at the collector are more difficult to quantify using only this probe. For magnetron discharge and rf plasmas the theoretical model differs significantly from the measurements. To estimate the individual contributions to the EFD, approximations using simulation have to be made. Here, for example, the RFTP can be a useful link between simulations and ex-situ examined films.

All in all, the RFTP diagnostic presented here proves a valuable addition to the field of plasma probe diagnostics, since it gives new insight into the energy balance of species in the plasma by differentiating between ions and neutrals. For future endeavours, it could be used to study secondary electron emission of different materials by changing the PTP/collector material. With suitable electronics, the probe could be embedded into the driven electrode of an rf plasma and investigate the effect of the typical two-peaked IED on the energy flux density. Also, HiPIMS processes could be looked at in more detail when the probe is able to resolve a single pulse.

Acknowledgements
The magnetron discharge measurements were done at the Surface Science & Coating Technologies Group at Empa, Switzerland. The authors thank Kerstin Thorwarth and Sebastian Siol for their assistance and the provision of the experimental setup.

Funding
Open Access funding enabled and organized by Projekt DEAL. This work was not funded by any third party.

Availability of data and materials
The data that support the findings in this study are available from the corresponding author upon reasonable request.

Declarations

Competing interests
The authors declare that they have no competing interests.

Author contributions
FS: Conceptualization, Investigation, Analysis, Writing. HK: Conceptualization, Supervision. All authors have read and approved the final manuscript.

Received: 3 May 2023 Accepted: 3 November 2023 Published online: 15 November 2023

References

1. Benedikt J, Kersten H, Piel A. Foundations of measurement of electrons, ions and species fluxes towards surfaces in low-temperature plasmas. Plasma Sources Sci Technol. 2021;30(3):033001. https://doi.org/10.1088/1361-6595/abe4bf.
2. Hanna AR, Fisher ER. Investigating recent developments and applications of optical plasma spectroscopy: a review. J Vac Sci Technol A. 2020;38(2):020806. https://doi.org/10.1116/1.5141844.
3. Benedikt J, Hecimovic A, Ellerweg D, von Keudell A. Quadrupole mass spectrometry of reactive plasmas. J Phys D, Appl Phys. 2012;45(40):403001. https://doi.org/10.1088/0022-3727/45/40/403001.
4. Demidov VI, Ratynskaia SV, Rypdal K. Electric probes for plasmas: the link between theory and instrument. Rev Sci Instrum. 2002;73(10):3409–39. https://doi.org/10.1063/1.1505099.
5. Spethmann A, Trottenberg T, Kersten H, Hey FG, Grimaud L, Mazouffre S, Bock D, Tajmar M. Force probes for development and testing of different electric propulsion systems. EPJ Tech Instrum. 2022;9(1):4. https://doi.org/10.1140/epjti/s40485-022-00079-w.
6. Klindworth M, Arp O, Piel A. Langmuir probe diagnostics in the IMPF device and comparison with simulations and tracer particle experiments. J Phys D, Appl Phys. 2006;39(6):1095–104. https://doi.org/10.1088/0022-3727/39/6/015.
7. Singh SB, Chand N, Patil DS. Langmuir probe diagnostics of microwave electron cyclotron resonance (ECR) plasma. Vacuum. 2008;83(2):372–7. https://doi.org/10.1016/j.vacuum.2008.05.030.
8. Irimiciuc SA, Chertopalov S, Lancok J, Craciun V. Langmuir probe technique for plasma characterization during pulsed laser deposition process. Coatings. 2021;11(7):762. https://doi.org/10.3390/coatings11070762.
9. Piejak RB, Godyak VA, Garner R, Alexandrovich BM, Sternberg N. The hairpin resonator: a plasma density measuring technique revisited. J Appl Phys. 2004;95(7):3785–91. https://doi.org/10.1063/1.1652247.
10. Lovberg RH. The use of magnetic probes in plasma diagnostics. Ann Phys. 1959;8(3):311–24. https://doi.org/10.1016/0003-4916(59)90001-6.
11. Gahan D, Dolinaj B, Hopkins MB. Comparison of plasma parameters determined with a Langmuir probe and with a retarding field energy analyzer. Plasma Sources Sci Technol. 2008;17(3):035026. https://doi.org/10.1088/0963-0252/17/3/035026.
12. Meister H, Bernert M, Biel W, Han M, Ingesson LC, Mukai K, Penzel F, Peterson BJ, Reichle R, Reinke ML, Schmitt S, Zhang D. Bolometer developments in diagnostics for magnetic confinement fusion. J Instrum. 2019;14(10):10004. https://doi.org/10.1088/1748-0221/14/10/C10004.
13. Thornton JA. Substrate heating in cylindrical magnetron sputtering sources. Thin Solid Films. 1978;54(1):23–31. https://doi.org/10.1016/0040-6090(78)90273-0.
14. van den Berg-Stolp J, Classen IGJ, van der Meiden HJ, Vernimmen JWM, Brons S, van Rooij GJ. Inducing thermionic emission from lanthanum hexaboride probes in magnum-PSI. Nucl Mater Energy. 2021;29:101097. https://doi.org/10.1016/j.nme.2021.101097.
15. Schneider V, Kersten H. An optical trapping system for particle probes in plasma diagnostics. Rev Sci Instrum. 2018;89(10):103505. https://doi.org/10.1063/1.5051065.
16. Hübner S, Palomares JM, Carbone EAD, van der Mullen JJAM. A power pulsed low-pressure argon microwave plasma investigated by Thomson scattering: evidence for molecular assisted recombination. J Phys D, Appl Phys. 2012;45(5):055203. https://doi.org/10.1088/0022-3727/45/5/055203.
17. Vaudolon J, Mazouffre S. Indirect determination of the electric field in plasma discharges using laser-induced fluorescence spectroscopy. Phys Plasmas. 2014;21(9):093505. https://doi.org/10.1063/1.4895532.
18. Dittmann K, Küllig C, Meichsner J. 160 GHz Gaussian beam microwave interferometry in low-density rf plasmas. Plasma Sources Sci Technol. 2012;21(2):024001. https://doi.org/10.1088/0963-0252/21/2/024001.
19. Baloniak T, Reuter R, Flötgen C, von Keudell A. Calibration of a miniaturized retarding field analyzer for low-temperature plasmas: geometrical transparency and collisional effects. J Phys D, Appl Phys. 2010;43(5):055203. https://doi.org/10.1088/0022-3727/43/5/055203.
20. Böhm C, Perrin J. Retarding-field analyzer for measurements of ion energy distributions and secondary electron emission coefficients in low-pressure radio frequency discharges. Rev Sci Instrum. 1993;64(1):31–44. https://doi.org/10.1063/1.1144398.

21. Enloe CL. High-resolution retarding potential analyzer. Rev Sci Instrum. 1994;65(2):507–8. https://doi.org/10.1063/1.1145167.
22. Sharma S, Gahan D, Kechkar S, Daniels S, Hopkins MB. A spatially resolved retarding field energy analyzer design suitable for uniformity analysis across the surface of a semiconductor wafer. Rev Sci Instrum. 2014;85(4):043509. https://doi.org/10.1063/1.4870900.
23. Gauter S, Haase F, Kersten H. Experimentally unraveling the energy flux originating from a DC magnetron sputtering source. Thin Solid Films. 2019;669:8–18. https://doi.org/10.1016/j.tsf.2018.10.021.
24. Stahl M, Trottenberg T, Kersten H. A calorimetric probe for plasma diagnostics. Rev Sci Instrum. 2010;81(2):023504. https://doi.org/10.1063/1.3276707.
25. Gauter S, Fröhlich M, Garkas W, Polak M, Kersten H. Calorimetric probe measurements for a high voltage pulsed substrate (PBII) in a HiPIMS process. Plasma Sources Sci Technol. 2017;26(6):065013. https://doi.org/10.1088/1361-6595/aa6f9e.
26. Sahu BB, Yin Y, Gauter S, Han JG, Kersten H. Plasma engineering of silicon quantum dots and their properties through energy deposition and chemistry. Phys Chem Chem Phys. 2016;18(37):25837–51. https://doi.org/10.1039/C6CP05647D.
27. Zahari F, Schlichting F, Strobel J, Dirkmann S, Cipo J, Gauter S, Trieschmann J, Marquardt R, Haberfehlner G, Kothleitner G, Kienle L, Mussenbrock T, Ziegler M, Kersten H, Kohlstedt H. Correlation between sputter deposition parameters and I-V characteristics in double-barrier memristive devices. J Vac Sci Technol B. 2019;37(6):061203. https://doi.org/10.1116/1.5119984.
28. Lundin D, Stahl M, Kersten H, Helmersson U. Energy flux measurements in high power impulse magnetron sputtering. J Phys D, Appl Phys. 2009;42(18):185202. https://doi.org/10.1088/0022-3727/42/18/185202.
29. Hansen L, Kohlmann N, Kienle L, Kersten H. Correlations between energy flux and thin film modifications in an atmospheric pressure direct current microplasma. Thin Solid Films. 2023;765:139633. https://doi.org/10.1016/j.tsf.2022.139633.
30. Zeuner M, Scholze F, Neumann H, Chassé T, Otto G, Roth D, Hellmich A, Ocker B. A unique ecr broad beam source for thin film processing. Surf Coat Technol. 2001;142–144:11–20. https://doi.org/10.1016/S0257-8972(01)01144-6.
31. Trottenberg T, Schneider V, Kersten H. Measurement of the force on microparticles in a beam of energetic ions and neutral atoms. Phys Plasmas. 2010;17(10):103702. https://doi.org/10.1063/1.3489795.
32. Spethmann A, Trottenberg T, Kersten H. Instrument for spatially resolved simultaneous measurements of forces and currents in particle beams. Rev Sci Instrum. 2015;86(1):015107. https://doi.org/10.1063/1.4905534.
33. Phelps AV. The application of scattering cross sections to ion flux models in discharge sheaths. J Appl Phys. 1994;76(2):747–53. https://doi.org/10.1063/1.357820.
34. Spethmann A, Trottenberg T, Kersten H. Spatially resolved momentum flux measurements for thruster plume diagnostics. 2013.
35. Sarakinos K, Alami J, Konstantinidis S. High power pulsed magnetron sputtering: a review on scientific and engineering state of the art. Surf Coat Technol. 2010;204(11):1661–84. https://doi.org/10.1016/j.surfcoat.2009.11.013.
36. Seeger S, Harbauer K, Ellmer K. Ion-energy distributions at a substrate in reactive magnetron sputtering discharges in ar/h2s from copper, indium, and tungsten targets. J Appl Phys. 2009;105(5):053305. https://doi.org/10.1063/1.3086618.
37. Rudolph M, Lundin D, Foy E, Debongnie M, Hugon M-C, Minea T. Influence of backscattered neutrals on the grain size of magnetron-sputtered TaN thin films. Thin Solid Films. 2018;658:46–53. https://doi.org/10.1016/j.tsf.2018.05.027.
38. Schell V, Müller C, Durdaut P, Kittmann A, Thormählen L, Lofink F, Meyners D, Höft M, McCord J, Quandt E. Magnetic anisotropy controlled fecosib thin films for surface acoustic wave magnetic field sensors. Appl Phys Lett. 2020;116(7):073503. https://doi.org/10.1063/1.5140562.
39. Farhadizadeh A, Kozák T. The importance of discharge voltage in DC magnetron sputtering for energy of sputtered and backscattered atoms on the substrate: Monte-Carlo simulations. Vacuum. 2022;196:110716. https://doi.org/10.1016/j.vacuum.2021.110716.
40. Anders A. A structure zone diagram including plasma-based deposition and ion etching. Thin Solid Films. 2010;518(15):4087–90. https://doi.org/10.1016/j.tsf.2009.10.145.
41. Gudmundsson JT. Physics and technology of magnetron sputtering discharges. Plasma Sources Sci Technol. 2020;29(11):113001. https://doi.org/10.1088/1361-6595/abb7bd.
42. Bultinck E, Bogaerts A. Particle-in-cell/Monte Carlo collisions treatment of an Ar/O_2 magnetron discharge used for the reactive sputter deposition of TiO_x films. New J Phys. 2009;11(10):103010. https://doi.org/10.1088/1367-2630/11/10/103010.
43. Ellmer K, Welzel T. Reactive magnetron sputtering of transparent conductive oxide thin films: role of energetic particle (ion) bombardment. J Mater Res. 2012;27(5):765–79. https://doi.org/10.1557/jmr.2011.428.

Publisher's Note